Journal of Applied Physics

Phase-field modeling and electronic structural analysis of flexoelectric effect at 180° domain walls in ferroelectric $PbTiO_3$

Cite as: J. Appl. Phys. **122**, 224101 (2017); https://doi.org/10.1063/1.5017219
Submitted: 04 May 2017 . Accepted: 24 November 2017 . Published Online: 11 December 2017

Yu-Jia Wang, Jiangyu Li, Yin-Lian Zhu, and Xiu-Liang Ma

Phase-field modeling and electronic structural analysis of flexoelectric effect at 180° domain walls in ferroelectric $PbTiO_3$

Yu-Jia Wang,[1] Jiangyu Li,[2,3,a)] Yin-Lian Zhu,[1] and Xiu-Liang Ma[1,4,a)]
[1]*Shenyang National Laboratory for Materials Science, Institute of Metal Research, Chinese Academy of Sciences, 72 Wenhua Road, Shenyang, Liaoning 110016, China*
[2]*Shenzhen Key Laboratory of Nanobiomechanics, Shenzhen Institutes of Advanced Technology, Chinese Academy of Sciences, University Town of Shenzhen, Shenzhen, Guangdong 518055, China*
[3]*Department of Mechanical Engineering, University of Washington, Seattle, Washington 98195-2600, USA*
[4]*School of Materials Science and Engineering, Lanzhou University of Technology, Langongping Road 287, 730050 Lanzhou, China*

(Received 4 May 2017; accepted 24 November 2017; published online 11 December 2017)

The flexoelectric effect is the coupling between strain, polarization, and their gradients, which are prominent at the nanoscale. Although this effect is important to understand nanostructures, such as domain walls in ferroelectrics, its electronic mechanism is not clear. In this work, we combined phase-field simulations and first-principles calculations to study the 180° domain walls in tetragonal ferroelectric $PbTiO_3$ and found that the source of Néel components is the gradient of the square of spontaneous polarization. Electronic structural analysis reveals that there is a redistribution of electronic charge density and potential around domain walls, which produces the electric field and Néel components. This work thus sheds light on the electronic mechanism of the flexoelectric effect around 180° domain walls in tetragonal ferroelectrics. *Published by AIP Publishing.*
https://doi.org/10.1063/1.5017219

I. INTRODUCTION

Flexoelectricity describes the class of physical phenomena where the strain (stress) gradient induces electric polarization (field) or the electric polarization (field) gradient results in strain (stress). Recently, many studies investigated the effect of flexoelectricity on materials' properties, especially in ferroelectrics.[1–15] Abundant interfaces exist in ferroelectric materials, such as domain walls (DWs) and morphotropic phase boundaries (MPBs), which provide natural places where gradients in polarization and/or strain (stress) arise. Thus, the flexoelectric effect should be prominent at these interfaces. Indeed, many interesting properties of ferroelectric DWs or MPBs are found to be related to the flexoelectric effect. For example, Catalan *et al*. found that there exists a strain distribution around the 90° DW near the substrate in $PbTiO_3$ (PTO) films, which causes polarization rotations through the flexoelectric effect.[3] The normally uncharged DWs in $BiFeO_3$ and $Pb(Zr,Ti)O_3$ are found to be conductive,[16,17] which may be caused by the Néel-type polarization components due to the flexoelectric effect.[18] The MPB between R-like and T-like $BiFeO_3$ shows many interesting properties, such as high piezoelectric and magnetic responses[19] and a large enhancement in the anisotropic interfacial photocurrent,[12] which may be explained by considering the flexoelectric effect as well.[20]

180° DWs in tetragonal ferroelectrics are generally 1–2 nm thick, near which large polarization and strain gradients exist. Thus, the flexoelectric effect is very important to understand the structure of 180° DWs. The main feature of a 180° DW is its tangential polarization profile: The polarization vectors rapidly shrink their magnitudes near DWs and reverse their directions upon crossing DW planes. Accompanying such a polarization profile, there is also a strain distribution due to the electrostrictive effect. This is the classical Ising-type 180° DWs. Recent studies, however, showed that the structures of 180° DWs are far more complex. Besides the Ising-type components, other components of Bloch- and Néel-type could also exist around 180° DWs.[21–28] Phenomenological analysis and phase-field simulations indicate that the flexoelectric effect should be taken into account to understand the emergence of these non-Ising characters.[26–28] However, it is not clear how these components actually emerge, especially at the electronic level.

In this paper, with the aim to understand the importance of flexoelectricity on 180° DWs and its electronic mechanisms, we first used phase-field simulations to study the effects of flexoelectric coefficients on the structure of 180° DWs and then used first-principles calculations to further understand the electronic origin of the flexoelectric effect, taking the [100]-oriented 180° DW in PTO as an example. We found that the source of Néel components is the gradient of the square of spontaneous polarization. Electronic structural analysis reveals that a redistribution of electronic charge density and potential spontaneously emerges around DWs, which produces the electric field between the DW region and the bulk region and finally induces Néel components.

II. CALCULATION METHODS

A. Phase-field model

3D phase-field models are developed to study the effect of flexoelectricity on the polarization and strain characteristics around DWs in tetragonal ferroelectrics. The order

a)Authors to whom correspondence should be addressed: jjli@uw.edu and xlma@imr.ac.cn

parameters are chosen as the three components of polarization vectors. The system energy is the functional of polarization and strain

$$F = F_{bulk} + F_{grad} + F_{elas} + F_{elec}. \tag{1}$$

The first term is the bulk energy or Landau-Devonshire energy

$$\begin{aligned} F_{bulk} = {} & \alpha_1\left(P_1^2 + P_2^2 + P_3^2\right) + \alpha_{11}\left(P_1^4 + P_2^4 + P_3^4\right) \\ & + \alpha_{12}\left(P_1^2P_2^2 + P_2^2P_3^2 + P_3^2P_1^2\right) + \alpha_{111}\left(P_1^6 + P_2^6 + P_3^6\right) \\ & + \alpha_{112}\left[P_1^4\left(P_2^2 + P_3^2\right) + P_2^4\left(P_3^2 + P_1^2\right) + P_3^4\left(P_1^2 + P_2^2\right)\right] \\ & + \alpha_{123}P_1^2P_2^2P_3^2, \end{aligned} \tag{2}$$

which could be used to describe a first order ferroelectric phase transition.

The second term is the gradient energy or Ginzburg energy, whose contribution to the total system is reflected as the DW energy

$$\begin{aligned} F_{grad} = {} & \frac{1}{2}G_{11}(P_{1,1}^2 + P_{2,2}^2 + P_{3,3}^2) + G_{12}(P_{1,1}P_{2,2} \\ & + P_{2,2}P_{3,3} + P_{3,3}P_{1,1}) + \frac{1}{2}G_{44}[(P_{1,2} + P_{2,1})^2 \\ & + (P_{2,3} + P_{3,2})^2 + (P_{3,1} + P_{1,3})^2]. \end{aligned} \tag{3}$$

The third term is the elastic energy

$$F_{elas} = \frac{1}{2}C_{ijkl}e_{ij}e_{kl} = \frac{1}{2}C_{ijkl}(\varepsilon_{ij} - \varepsilon_{ij}^o - \varepsilon_{ij}^f)(\varepsilon_{kl} - \varepsilon_{kl}^o - \varepsilon_{kl}^f), \tag{4}$$

where C_{ijkl} is the elastic stiffness tensor and e_{ij}, ε_{ij}, ε_{ij}^o, and ε_{ij}^f are the elastic strain, the total strain, the electrostrictive strain, and the flexoelectric strain. The electrostrictive and flexoelectric strains can be calculated by the following equations:

$$\varepsilon_{ij}^o = Q_{ijkl}P_kP_l, \tag{5a}$$

$$\varepsilon_{ij}^f = -F_{ijkl}P_{k,l}, \tag{5b}$$

where Q_{ijkl} and F_{ijkl} are the electrostrictive and flexoelectric coefficients. In Eq. (4), we incorporate the electrostrictive and flexoelectric effects into the elastic energy. As demonstrated in the supplementary material, this expression is the Legendre transformation of the corresponding terms in the elastic Gibbs free energy.

The fourth term is the electrostatic energy

$$F_{elec} = -\frac{1}{2}E_i^{dep}P_i, \tag{6}$$

where E_i^{dep} is the depolarization field.

By differentiating these energies with respect to the polarization, we can get the forces to drive the evolution of polarization. Among these forces, the mechanical driving force must be handled carefully and the result is

$$-\frac{\delta F_{elas}}{\delta P_i} = 2q_{ijkl}P_je_{kl} + f_{ijkl}e_{kl,j}, \tag{7}$$

where $q_{ijkl} = C_{ijmn}Q_{mnkl}$ and $f_{ijkl} = C_{ijmn}F_{mnkl}$ are other types of electrostrictive and flexoelectric coefficients. From this expression, we can see that both the elastic strains and their gradients contribute to the mechanical driving force. The derivation can be found in the supplementary material. One term in the elastic strain gradient is the second-order derivative of the polarization, which will renormalize the gradient coefficient in Eq. (3). These renormalized gradient coefficients depend on the sign and magnitude of flexoelectric coefficients. As demonstrated in the supplementary material, these coefficients can be safely omitted in our study.

Since this mechanical driving force is effectively an electric field, the two terms in this equation can be considered as the electrostriction-induced and flexoelectricity-induced electric fields. The key term in Eq. (7) is the elastic strain, which can be obtained by solving the mechanical equilibrium equation [Eq. (8a)]. The depolarization field can be found by solving the Poisson's equation [Eq. (8b)]. After all the driving forces are found, the Ginzburg-Landau equation [Eq. (8c)] can be solved to update the polarization vectors.

$$\sigma_{ij,j} = 0, \tag{8a}$$

$$D_{i,i} = 0, \tag{8b}$$

$$\frac{\partial P_i}{\partial t} = -L\frac{\delta F}{\delta P_i}, \tag{8c}$$

where D is the electric displacement and L is the dynamical parameter.

A grid of $4096 \times 2 \times 2$ was used to simulate the 180° DW model, where each grid point corresponds to 0.2 nm. The normal of 180° DWs is parallel to the x direction. In the initial structure, the polarizations of one half of grid points are set along the $+z$ direction while the other half along the $-z$ direction. The three-dimensional periodic boundary condition is applied and the fast Fourier transformation is adopted to solve Eqs. (8a)–(8c). By solving the mechanical equilibrium equation, we found that σ_{11}, σ_{12}, σ_{13}, and σ_{23} are all zero, while σ_{22} and σ_{33} are non-zero close to DWs and approach to zero away from DWs. Thus, our boundary condition is consistent with the stress-free boundary condition ($\sigma_{ij}|_{x\to\pm\infty} = 0$). The simulation was considered to be convergent when the averaged polarization difference between two sequential simulation steps is less than 1×10^{-8}. The material parameters of PTO are adopted from the previous literature.[29] The gradient coefficients are chosen to make the DW width the same as the first-principles result. All the coefficients are listed in Table I.

B. First-principles calculation details

The atomic relaxation and electronic structure calculation were performed by Vienna ab-initio simulation package (VASP).[30,31] The energy cutoff was chosen as 550 eV, and the local density approximation was used with the method of projector augmented-wave.[32] The O 2s2p, Ti 3s3p3d4s, and Pb 5d6s6p electrons are treated as the valence electrons. The optimized lattice constants a and c of PTO are 3.867 and 4.033 Å, respectively, consistent with previous calculation results.[21,22]

TABLE I. Material parameters of $PbTiO_3$.[29]

$\alpha_1 = -1.73 \times 10^8\ C^{-2}\cdot m^2\cdot N$	$\alpha_{11} = -7.3 \times 10^7\ C^{-4}\cdot m^6\cdot N$	$\alpha_{12} = 7.5 \times 10^8\ C^{-4}\cdot m^6\cdot N$
$\alpha_{111} = 2.6 \times 10^8\ C^{-6}\cdot m^{10}\cdot N$	$\alpha_{112} = 6.1 \times 10^8\ C^{-6}\cdot m^{10}\cdot N$	$\alpha_{123} = -3.7 \times 10^9\ C^{-6}\cdot m^{10}\cdot N$
$G_{11} = 4.8 \times 10^{-11}\ C^{-2}\cdot m^4\cdot N$	$G_{12} = -4.8 \times 10^{-11}\ C^{-2}\cdot m^4\cdot N$	$G_{44} = 4.8 \times 10^{-11}\ C^{-2}\cdot m^4\cdot N$
$C_{11} = 1.75 \times 10^{11}\ N\cdot m^{-2}$	$C_{12} = 7.94 \times 10^{10}\ N\cdot m^{-2}$	$C_{44} = 1.11 \times 10^{11}\ N\cdot m^{-2}$
$Q_{11} = 0.089\ C^{-2}\cdot m^4$	$Q_{12} = -0.026\ C^{-2}\cdot m^4$	$Q_{44} = 0.034\ C^{-2}\cdot m^4$
$\alpha_0 = 1.73 \times 10^8\ C^{-2}\cdot m^2\cdot N$	$G_{110} = 6.9 \times 10^{-12}\ C^{-2}\cdot m^4\cdot N$	$P_0 = 0.76\ C\cdot m^{-2}$

The 180° DW models were built by aligning several oppositely oriented tetragonal unit cells along the x direction. We chose $Nx = 12$, which is large enough to simulate the domain structure of PTO, according to our previous study.[33] These lattice parameters were fixed during the atomic relaxation to obtain the optimized 180° DW models. The k-point mesh was chosen as $1 \times 6 \times 6$. The ionic relaxation was considered as convergent when the Hellmann-Feynman (HF) force on each ion is less than 2 meV/Å. The polarization of each unit cell in the 180° DW model can be calculated by the Born effective charge method.[33,34]

III. RESULTS AND DISCUSSION

A. The effect of flexoelectric coefficients

For materials with cubic symmetry, there are three nonzero independent flexoelectric coefficients: f_{1111}, f_{1122}, and f_{1212}, which are abbreviated as f_{11}, f_{12}, and f_{44} ($f_{44} = 2f_{1212}$) using the Voigt's notation. We performed several testing calculations by individually setting one of the three coefficients as positive and negative values and keeping the other two zero. Since the flexoelectric coefficients of PTO are unknown, we chose them arbitrarily. The results are listed in Table II. It is found that when the flexoelectric effect is not taken into account, there are no induced Néel components, and when flexoelectric coefficients change sign, the direction of Néel components also changes. Only f_{11} and f_{12} contribute to the formation of Néel components, while f_{44} has no effects. From Table II, it is found that the maximum Néel component induced by f_{11} is one order of magnitude smaller than that induced by f_{12} when $f_{11} = f_{12}$. Considering that f_{11} is also one order of magnitude smaller than f_{12} for many perovskite oxides,[35] the main contribution can be ascribed to f_{12}. As shown in Sec. III B, the first-principles-calculated Néel component in the Ising-Néel DW is tail-to-tail, which indicates that f_{12} is negative for PTO. The polarization distribution around the DW in the case of $f_{12} = -10$ (the normalized value, equivalent to −0.26 V) is shown in Fig. 1.

TABLE II. Maximal Néel-type polarizations and the nature of the induced Néel polarization profile at different combinations of flexoelectric coefficients obtained from phase-field simulations.

Flexoelectric coefficients (normalized value)	Max. Néel component (unit: P_s)	Néel polarization profile
$f_{11} = f_{12} = f_{44} = 0$	0	-
$f_{11} = +10, f_{12} = f_{44} = 0$	6.4×10^{-3}	Tail-to-tail
$f_{11} = -10, f_{12} = f_{44} = 0$		Head-to-head
$f_{12} = +10, f_{11} = f_{44} = 0$	1.4×10^{-2}	Head-to-head
$f_{12} = -10, f_{11} = f_{44} = 0$		Tail-to-tail
$f_{44} = \pm 10, f_{11} = f_{12} = 0$	0	-

The effect of f_{11} and f_{12} can be understood by the flexoelectric field in the x direction

$$E_1 = f_{1jkl}e_{kl,j} = f_{11}e_{11,1} + f_{12}(e_{22,1} + e_{33,1}). \tag{9}$$

The elastic strain components read

$$e_{11} = \varepsilon_{11} - \varepsilon_{11}^o - \varepsilon_{11}^f = \varepsilon_{11} - Q_{11}P_1^2 - Q_{12}P_2^2 - Q_{12}P_3^2 + F_{11}P_{1,1} + F_{12}P_{2,2} + F_{12}P_{3,3} \approx \varepsilon_{11} - Q_{12}P_3^2, \tag{10a}$$

$$e_{22} = \varepsilon_{22} - \varepsilon_{22}^o - \varepsilon_{22}^f = \varepsilon_{22} - Q_{12}P_1^2 - Q_{11}P_2^2 - Q_{12}P_3^2 + F_{12}P_{1,1} + F_{11}P_{2,2} + F_{12}P_{3,3} \approx \varepsilon_{22} - Q_{12}P_3^2, \tag{10b}$$

$$e_{33} = \varepsilon_{33} - \varepsilon_{33}^o - \varepsilon_{33}^f = \varepsilon_{33} - Q_{12}P_1^2 - Q_{12}P_2^2 - Q_{11}P_3^2 + F_{12}P_{1,1} + F_{12}P_{2,2} + F_{11}P_{3,3} \approx \varepsilon_{33} - Q_{11}P_3^2. \tag{10c}$$

We have drawn the distributions of total strains and elastic strains, as presented in Fig. 2. The distributions of stresses are also shown in this figure. It is found that the total strains ε_{22} and ε_{33} are constant and the variance of ε_{11} is very small. As a contrast, large gradients of elastic strains exist around DWs. Inserting the formulae of elastic strain into Eq. (9), the electric field in the x direction can be written as

$$E_1 \approx -[f_{11}Q_{12} + f_{12}(Q_{11} + Q_{12})]\left(P_3^2\right)_{,1}. \tag{11}$$

This equation is consistent with the previous literature,[28] which indicates that the omission of several terms in Eqs. (10a)–(10c) is legitimate. According to the above analysis, the term containing f_{11} could be further omitted. Since

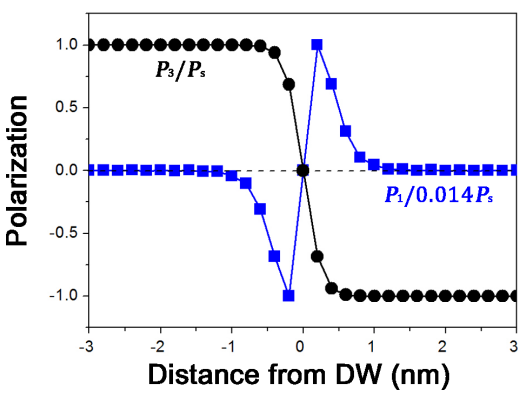

FIG. 1. The polarization profiles around a 180° DW in PTO obtained from the phase-field simulation with $f_{12} = -10$. P_s is 0.76 C/m^2.

$Q_{11}+Q_{12}$ is positive[29] and f_{12} is negative for PTO, Eq. (11) can be written as

$$E_1 = A\left(P_3^2\right)_{,1}, \tag{12}$$

where A is a positive number.

In Fig. 3, the flexoelectric field and the depolarization field are plotted. The distribution of the flexoelectric field depends on the sign of the flexoelectric coefficients. In our studied case, f_{12} is negative. As a result, the flexoelectric field forms a tail-to-tail distribution, while the depolarization field forms a head-to-head distribution. The flexoelectric field is much stronger than the depolarization field. The final distribution of Néel components is the competition result of the flexoelectric and depolarization fields, also a tail-to-tail distribution.

B. Electronic structural analysis of flexoelectricity at 180° domain walls

To understand the flexoelectric effect around 180° DWs more deeply, first-principles calculations were performed. For ferroelectric PTO, it is predicted by first-principles calculations that large Bloch components comparable to Ising ones could develop at [100]-oriented 180° DWs, resulting in a ferroelectric transition at ferroelectric DWs.[33,36] Both Ising and Bloch polarization profiles may induce Néel components through the flexoelectric effect. Indeed, our previous study showed that the optimized (realistic) [100]-oriented 180° DW model is the Ising-Bloch-Néel (IBN) one.[33] However, phase-field simulations only predict the Ising-Néel (IN) character for [100]-oriented 180° DWs (see Sec. III A and Ref. 28). To make a comparison between phase-field and first-principles results, in this section, we first considered the artificial IN model, which is obtained by removing Bloch components in the IBN model. In Sec. III C, we further studied the realistic IBN model and another artificial model [the Bloch-Néel (BN) model], which is obtained by removing Ising components in the IBN model. Comparing the results of the artificial IN and BN models from those of the realistic IBN model could help us to understand the individual effect of Ising and Bloch polarization profiles on the induction of Néel components. Constrained relaxations were performed for the IN and BN models: Atoms are only allowed to move in the x direction.

Figure 4(a) gives the polarization distributions of Ising and Néel components in the IN model. The tail-to-tail distribution of Néel components is obtained and the peak value (0.57 μC/cm^2) is 0.7% of the bulk polarization (86.3 μC/cm^2). If we assume that only f_{12} contributes to the Néel components, we can estimate the magnitude of f_{12} by fitting the phase-field result with the first-principles one. The fitting result of f_{12} is about -0.13 V. The tail-to-tail distribution of Néel components means that there exists a bound charge around the 180° DW. The bound charge can be calculated according to the formula: $\rho^{\text{bound}} = -\nabla\cdot\boldsymbol{P}$, following the method of Li *et al.*[37] Fig. 4(b) gives the bound charge distribution of the DW model. It can be found that there exists a negatively charged region at the center of a DW and two positively charged regions nearby. The extreme values of negative and positive charges are about -3.0×10^7 C/m^3 and 1.6×10^7 C/m^3, respectively. They are about one order of magnitude larger than those around the 180° DW in $BaTiO_3$.[37] The reason may be that $PbTiO_3$ has larger spontaneous polarization and the induced Néel components are also larger.

To uncover the ultimate source of Néel components at the electronic level, we artificially removed ferroelectric displacements in the x direction (Néel), while kept those in the z direction (Ising). Then, the unit-cell-averaged electron charge

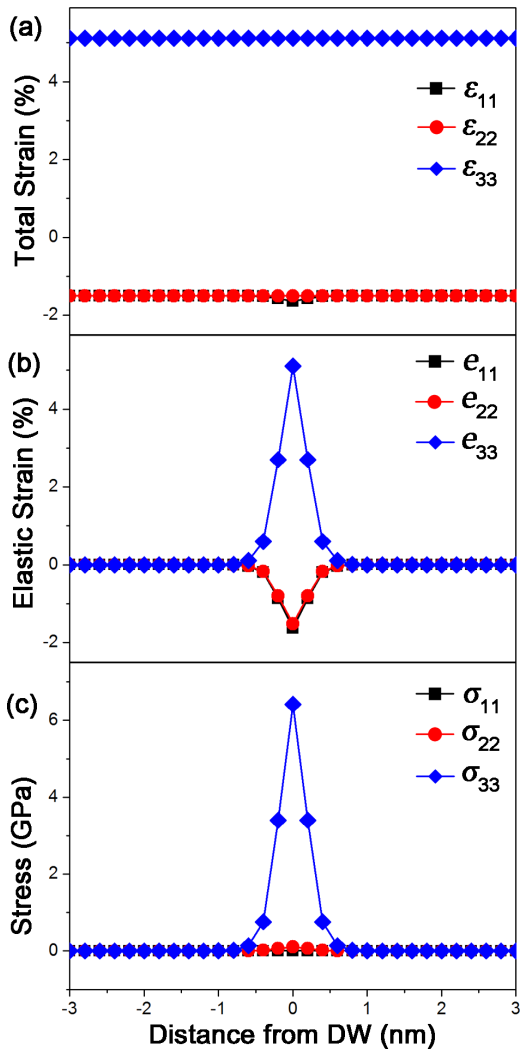

FIG. 2. The distributions of total strain, elastic strain, and stress around a 180° DW in PTO obtained from the phase-field simulation with $f_{12}=-10$.

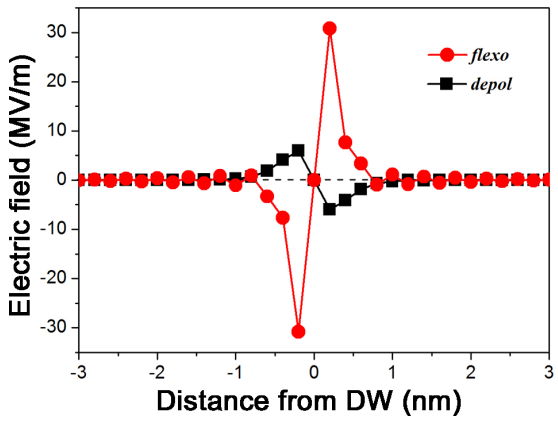

FIG. 3. The profiles of flexoelectric and depolarization fields around a 180° DW in PTO obtained from the phase-field simulation with $f_{12}=-10$.

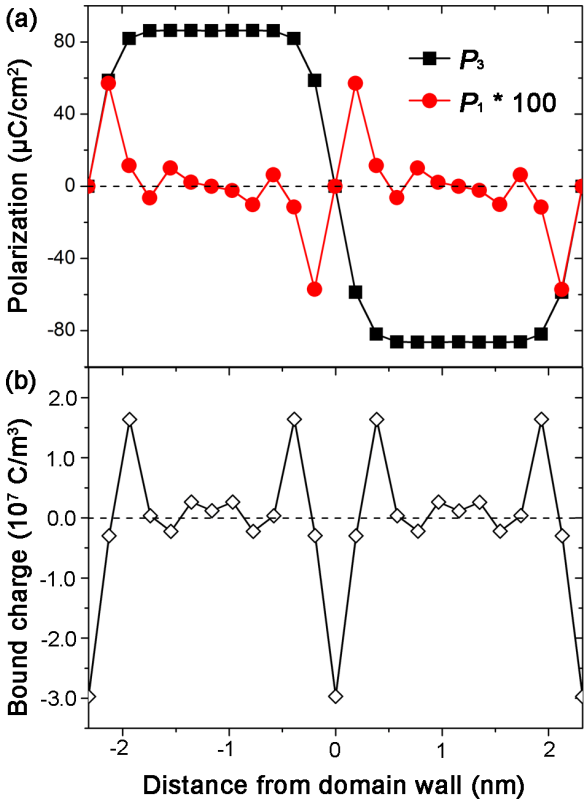

FIG. 4. (a) The polarization profiles around 180° DWs for the IN model obtained from first-principles calculations. (b) The bound charge distribution calculated from the Néel polarization distribution.

density and potential distributions along the x direction are calculated according to the method used in Ref. 34, as shown in Fig. 5. The distribution of the electric field component in the x direction is also shown by differentiating the potential with the x coordinate. From Fig. 5(a), we can see that there is an accumulation zone of positive charge localized in about one unit cell at the DW and two negative charged zones at both sides. The magnitudes of negative and positive charges in Fig. 5(a) are about -2.0×10^7 C/m^3 and 1.2×10^7 C/m^3, respectively, whose absolute values are in the same order of magnitude as the bound charges in Fig. 4(b). Due to the charge separation, a potential difference is built between the DW and the bulk region, as shown in Fig. 5(b). This potential difference will generate a tail-to-tail electric field distribution [Fig. 5(c)] and induce a tail-to-tail P_1 distribution. The maximal electric field could reach 3×10^8 V/m.

The result that there is a positive charge accumulation at Ising DWs seems to contradict the common knowledge that Ising DWs should be non-conductive. Actually, the charge density is obtained by fixing the atomic coordinates and doing the electronic optimization for the Ising DW model. As a result, there are no ionic polarizations in the x direction, while the electronic polarizations exist. Thus, the development of Neel components can be considered as a two-step process: First, electron redistribution spontaneously emerges in the Ising DW and a potential difference is built between the DW region and the bulk region; Second, ionic displacements normal to the DW are induced by this potential difference, resulting in Néel components.

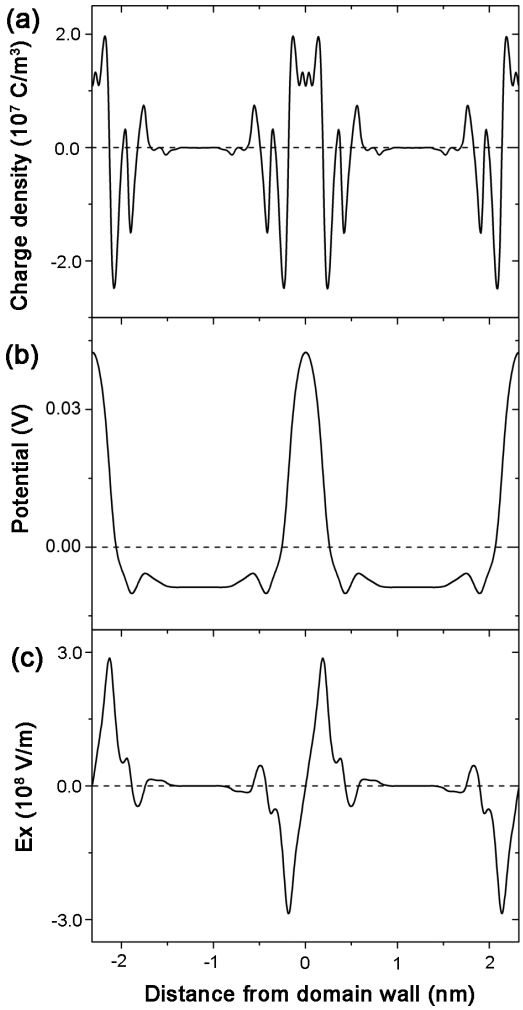

FIG. 5. The distribution of averaged charge density (a), potential (b) and electric field in the x direction (c) around 180° DWs for the IN model obtained from first-principles calculations.

Comparing Fig. 4(b) with Fig. 5(a), we can find that the two charge distributions show opposite trends. This observation could help us to understand the emergence of Néel components from another aspect: The gradient of the square of Ising components produces a nonuniformly distributed elastic strain (stress). As a result, a nonuniformly distributed charge density forms [Fig. 5(a)]. To compensate this charge density, Néel components develop with oppositely distributed bound charge [Fig. 4(b)].

C. The competition of Ising and Bloch components on the induction of Néel components

In Sec. III B, we considered the IN model, where Néel components are only induced by Ising components. In this section, we further considered the case that Néel components are only induced by Bloch components (the BN model) and the realistic case that Néel components are the combined result of both Ising and Bloch components (the IBN model).

Figures 6(a)–6(c) give the first-principles results of the BN model. It is found that head-to-head Néel components are induced, as shown in Fig. 6(a). In contrast, tail-to-tail Néel components are induced in the IN model, as shown in Fig. 4(a).

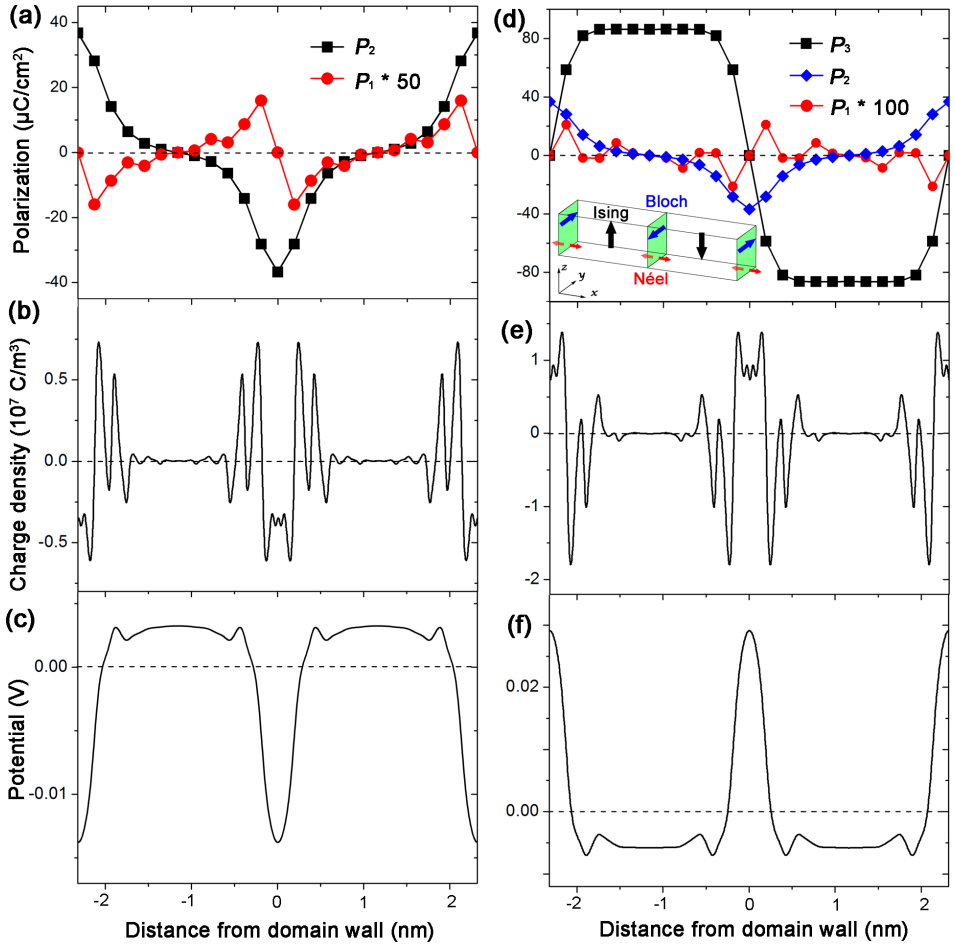

FIG. 6. The profiles of polarization, averaged charge density, and potential for the BN (left panel) and IBN (right panel) models obtained from first-principles calculations. The distributions of Ising, Bloch, and Néel components in the realistic IBN model are schematically shown as an inset in (d).

Following the same technique of Fig. 5, the Néel components are removed in the BN model and the unit-cell-averaged charge density and potential profiles are calculated, as shown in Figs. 6(b) and 6(c). It is found that DWs are the accumulation zones of negative charge and the potential valleys. Thus, head-to-head electric field and Néel polarization distributions are induced.

Figures 6(d)–6(f) give the first-principles results of the IBN model, where the induced Néel components adopt a tail-to-tail distribution [Fig. 6(d)], the same as the IN model. However, the magnitudes of Néel components are largely reduced compared with the IN model (peak values: 0.21 vs 0.57 μC/cm^2). From the corresponding profiles of charge density and potential shown in Figs. 6(e) and 6(f), it is found that DWs are the accumulation zones of positive charge and potential peaks.

Comparing the results of the three models, it is found that there exists a one-to-one relationship between the charge and potential distribution of the Néel-free DWs and the nature of the induced Néel polarization profile, as shown in Table III. These results provide more convincing evidence to the electronic origin of the flexoelectric effect at 180° DWs.

We can also understand the three models phenomenologically. The IN model has been studied in Sec. III A and the conclusion is that Néel components are induced by the gradient of the square of Ising components, as shown in Eq. (12). Following the same deduction from Eqs. (9) to (12), we can obtain two similar equations for the BN and IBN models

$$E_1 \approx A\left(P_2^2\right)_{,1}, \tag{13a}$$

$$E_1 \approx A\left(P_2^2 + P_3^2\right)_{,1}, \tag{13b}$$

where the coefficient A is the same positive number as the one in Eq. (12).

The distributions of P_2^2, P_3^2, $P_2^2 + P_3^2$, and their gradients are shown in Fig. 7. It is found that P_2^2 shows peaks at DWs, while both P_3^2 and $P_2^2 + P_3^2$ show valleys at DWs. As a result, the gradient of P_2^2 is head-to-head, while the gradients of P_3^2 and $P_2^2 + P_3^2$ are tail-to-tail. That is the reason why head-to-head Néel component distribution is observed in the BN model and tail-to-tail Néel component distribution in the IN and IBN models.

IV. CONCLUSIONS

In this work, we used phase-field simulations to study the effect of different flexoelectric coefficients on the distribution of Néel components around 180° DWs in tetragonal ferroelectric PTO and further used first-principles

TABLE III. The relationship between the charge and potential distribution of the Néel-free DWs and the nature of the induced Néel polarization profile in the three models.

Model	Charge at DWs	Potential at DWs	Néel polarization profile
IN	Positive	Peak	Tail-to-tail
BN	Negative	Valley	Head-to-head
IBN	Positive	Peak	Tail-to-tail

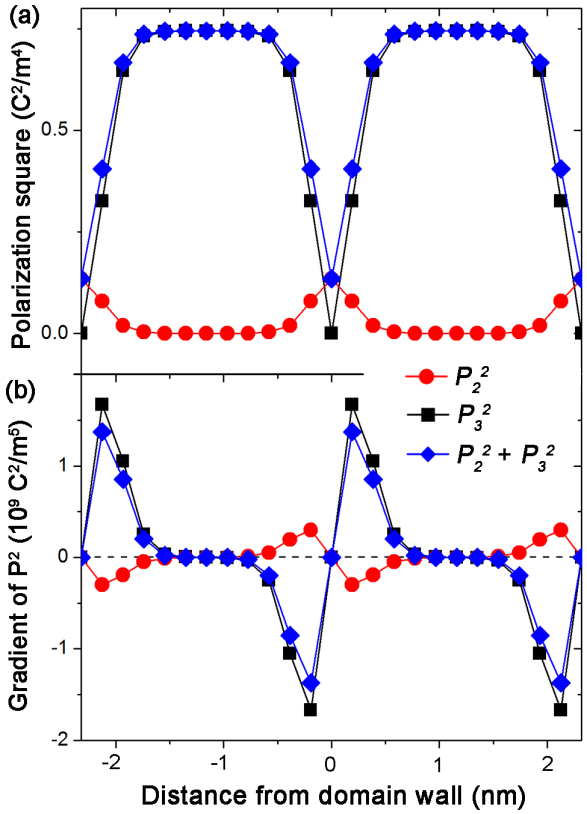

FIG. 7. The distributions of P_2^2, P_3^2, $P_2^2 + P_3^2$ (a), and their gradients (b) around 180° DWs in PTO obtained from first-principles calculations. The red, black, and blue curves correspond to the BN, IN, and IBN models.

calculations to explore the electronic origin of the flexoelectric effect. The main conclusions are listed as follows:

1. The driving force of Néel components comes from the flexoelectric coefficient f_{11} and f_{12} and the source of Néel components is the gradient of the square of spontaneous polarization.
2. Electronic structural analysis reveals that an accumulation zone of positive charge spontaneously emerges around the Ising type 180° DWs, which results in the potential difference, tail-to-tail electric field and Néel components.
3. The contributions of Ising and Bloch components in the [100]-oriented 180° DWs in PTO on the formation of Néel components are opposite and the competition result is also a tail-to-tail distribution of Néel components with reduced magnitudes, compared with Ising-Néel DWs.

SUPPLEMENTARY MATERIAL

See supplementary material for the deduction of Eqs. (4) and (7) and the discussion about the renormalized gradient coefficients.

ACKNOWLEDGMENTS

This work was supported by the National Key Basic Research Program of China (2016YFA0201001 and 2014CB921002), National Natural Science Foundation of China (Nos. 51401212, 11627801, 51571197, 51231007, 51671194, and 51521091), Key Research Program of Frontier Sciences CAS (QYZDJ-SSW-JSC010), Doctoral Initiation Foundation of Liaoning Province (No. 20141144), and Shenzhen Science and Technology Innovation Committee (JCYJ20170413152832151).

[1]P. Zubko, G. Catalan, A. Buckley, P. R. L. Welche, and J. F. Scott, Phys. Rev. Lett. **99**, 167601 (2007).
[2]I. Naumov, A. M. Bratkovsky, and V. Ranjan, Phys. Rev. Lett. **102**, 217601 (2009).
[3]G. Catalan *et al.*, Nat. Mater. **10**, 963 (2011).
[4]D. Lee, A. Yoon, S. Jang, J. G. Yoon, J. S. Chung, M. Kim, J. Scott, and T. Noh, Phys. Rev. Lett. **107**, 057602 (2011).
[5]H. Lu, C.-W. Bark, D. Esque de los Ojos, J. Alcala, C. B. Eom, G. Catalan, and A. Gruverman, Science **336**, 59 (2012).
[6]A. Y. Borisevich *et al.*, Nat. Commun. **3**, 775 (2012).
[7]B. C. Jeon *et al.*, Adv. Mater. **25**, 5643 (2013).
[8]Z. Wang, X. X. Zhang, X. Wang, W. Yue, J. Li, J. Miao, and W. Zhu, Adv. Funct. Mater. **23**, 124 (2013).
[9]T. D. Nguyen, S. Mao, Y.-W. Yeh, P. K. Purohit, and M. C. McAlpine, Adv. Mater. **25**, 946 (2013).
[10]P. Zubko, G. Catalan, and A. K. Tagantsev, Annu. Rev. Mater. Res. **43**, 387 (2013).
[11]A. Biancoli, C. M. Fancher, J. L. Jones, and D. Damjanovic, Nat. Mater. **14**, 224 (2015).
[12]K. Chu *et al.*, Nat. Nanotechnol. **10**, 972 (2015).
[13]Y. Gu, Z. Hong, J. Britson, and L.-Q. Chen, Appl. Phys. Lett. **106**, 022904 (2015).
[14]J. Narvaez, S. Saremi, J. Hong, M. Stengel, and G. Catalan, Phys. Rev. Lett. **115**, 037601 (2015).
[15]U. K. Bhaskar, N. Banerjee, A. Abdollahi, Z. Wang, D. G. Schlom, G. Rijnders, and G. Catalan, Nat. Nanotechnol. **11**, 263 (2016).
[16]J. Seidel *et al.*, Nat. Mater. **8**, 229 (2009).
[17]J. Guyonnet, I. Gaponenko, S. Gariglio, and P. Paruch, Adv. Mater. **23**, 5377 (2011).
[18]E. A. Eliseev, A. N. Morozovska, G. S. Svechnikov, P. Maksymovych, and S. V. Kalinin, Phys. Rev. B **85**, 045312 (2012).
[19]J. X. Zhang, R. J. Zeches, Q. He, Y. H. Chu, and R. Ramesh, Nanoscale **4**, 6196 (2012).
[20]C.-E. Cheng, H.-J. Liu, F. Dinelli, Y.-C. Chen, C.-S. Chang, F. S.-S. Chien, and Y.-H. Chu, Sci. Rep. **5**, 8091 (2015).
[21]D. Lee, R. Behera, P. Wu, H. Xu, Y. Li, S. B. Sinnott, S. Phillpot, L. Q. Chen, and V. Gopalan, Phys. Rev. B **80**, 060102 (2009).
[22]R. K. Behera, C.-W. Lee, D. Lee, A. N. Morozovska, S. B. Sinnott, A. Asthagiri, V. Gopalan, and S. R. Phillpot, J. Phys.-Condens. Matter **23**, 175902 (2011).
[23]J. Hlinka, V. Stepkova, P. Marton, I. Rychetsky, V. Janovec, and P. Ondrejkovic, Phase Transition **84**, 738 (2011).
[24]V. Stepkova, P. Marton, and J. Hlinka, J. Phys.-Condens. Matter **24**, 212201 (2012).
[25]M. Taherinejad, D. Vanderbilt, P. Marton, V. Stepkova, and J. Hlinka, Phys. Rev. B **86**, 155138 (2012).
[26]P. V. Yudin, A. K. Tagantsev, E. A. Eliseev, A. N. Morozovska, and N. Setter, Phys. Rev. B **86**, 134102 (2012).
[27]P. V. Yudin, A. K. Tagantsev, and N. Setter, Ferroelectrics **438**, 20 (2012).
[28]Y. Gu, M. Li, A. N. Morozovska, Y. Wang, E. A. Eliseev, V. Gopalan, and L.-Q. Chen, Phys. Rev. B **89**, 174111 (2014).
[29]Y. Li, S. Hu, Z. Liu, and L. Chen, Acta Mater. **50**, 395 (2002).
[30]G. Kresse and J. Furthmüller, Phys. Rev. B **54**, 11169 (1996).
[31]J. Hafner, Comput. Phys. Commun. **177**, 6 (2007).
[32]P. E. Blochl, Phys. Rev. B **50**, 17953 (1994).
[33]Y. J. Wang, D. Chen, Y. L. Tang, Y. L. Zhu, and X. L. Ma, J. Appl. Phys. **116**, 224105 (2014).
[34]B. Meyer and D. Vanderbilt, Phys. Rev. B **65**, 104111 (2002).
[35]R. Maranganti and P. Sharma, Phys. Rev. B **80**, 054109 (2009).
[36]J. C. Wojdeł and J. Íñiguez, Phys. Rev. Lett. **112**, 247603 (2014).
[37]M. Li, Y. Gu, Y. Wang, L.-Q. Chen, and W. Duan, Phys. Rev. B **90**, 054106 (2014).